OPTICAL SCATTERING AND MICROPHYSICAL PROPERTIES OF SUBVISUAL CIRRUS CLOUDS, AND CLIMATIC IMPLICATIONS

FINAL REPORT

Prepared for

National Aeronautics and Space Administration
Grant No. NAG-1-718
(1 December 1986 - 1 June 1988)

Prepared by

Kenneth Sassen, Michael K. Griffin and Gregory C. Dodd

Meteorology Department
University of Utah
Salt Lake City, Utah 84112

ABSTRACT

The optical and microphysical properties of subvisual cirrus clouds are derived from ground-based polarization lidar, shortwave radiation flux, and solar corona measurements of two ~0.75 km deep cirrus located near the tropopause. The first cloud produced no visual manifestations under excellent viewing conditions, and the second appeared to be a persistent aircraft contrail that was generally visible except in the zenith direction. Average lidar linear depolarization ratios and volume backscatter coefficients for the two clouds were 0.19 and 0.35, and 0.6×10^{-3} and 1.4×10^{-3} $(km\ sr)^{-1}$, respectively. It is estimated that the zenith-subvisual cirrus contained ice crystals of 25 μm effective diameter at a mean concentration of 25 ℓ^{-1} and ice mass content of 0.2 mg m^{-3}. The threshold cloud optical thickness for visual-versus-invisible cirrus, derived from both broadband shortwave flux and 0.694 μm lidar data, is found to be $\tau_c \approx 0.03$. Such τ values are comparable to those of 5-10 km deep stratospheric aerosol clouds of volcanic origin and polar stratospheric clouds, which are episodic in nature. Hence, we conclude that if these clouds are a fairly common feature of the upper troposphere, as recent SAGE satellite measurements would suggest, then the impact of natural and contrail subvisual cirrus on the planet's radiation balance may be relatively significant.

1. Introduction

With the advent of lidar atmospheric remote sensing, a practical but vaguely-defined category of cloud has emerged to describe an extended assembly of hydrometeors that is detected through laser backscattering and yet invisible to the unaided eye. Naturally, the existence of these "subvisual" clouds implies that the target has a comparatively low optical thickness, relative to some threshold value appropriate for a visible cloud. However, it is precisely this distinction that is ill-defined, since cloud visibility is based on the physiological perception of color and contrast, which depends on such factors as viewing geometry, the relative levels of background and target illumination, and the angular scattering patterns of the cloud particles. In contrast, the great returned signal dynamic range, power output, and spatial resolution capabilities of lidar permit the quantitative assessment of the properties of even a highly diffuse atmospheric target.

In recent years, the ability of lidar to quantify the properties of sub-visual targets has focused attention on the possible climatic effects of these weakly-scattering atmospheric layers. For example, from its inception, lidar has been used to study variations in stratospheric aerosol content, a phenomenon that can only be visually detected following a major volcanic injection of aerosols by a reddening of the sunrise or sunset sky, due to cumulative Mie scattering effects over a long atmospheric path length. Climatic modulations have been linked to the effects on radiative transfer of the elevated aerosol layers associated with volcanically-injected particles (Russell and Hake, 1977) and the newly-discovered polar stratospheric clouds (Pollack and McKay, 1985). Another candidate involves thin cirrus cloud layers composed of ice crystals often observed in the upper troposphere. Cirrus clouds are normally rather transparent, even to the point of being classified as "thin cirrus" when

the sky retains a bluish color in some viewing directions, but it is now recognized that cirrus can be present without any visual manifestations.

In this paper, the properties of upper-tropospheric ice clouds that are generally invisible to the naked eye are derived from polarization lidar, surface radiation flux, and solar corona photographic measurements. During the observation period, two separate cirrus cloud occurrences were studied. The first was not detected visually, and is termed a subvisual cirrus cloud. The second, a relatively narrow cirrus cloud band that was probably the remnants of an aircraft condensation trail (contrail), can be termed zenith-subvisual since, although it was invisible in the zenith viewing direction, it could be discerned when viewed at lower elevation angles and also as a result of the strong forward-scattering and corona effects it displayed in the vicinity of the solar disk. It follows that the observations provide an opportunity to assess the threshold cloud optical thickness value associated with visibility. Moreover, it is demonstrated that a cloud composed of ice crystals can produce the colored solar corona optical phenomenon previously associated only with liquid cloud droplet diffraction effects (Sassen, 1979).

The data were collected on 21 October 1986 from a site near Wausau in central Wisconsin (44.93° latitude and 89.63° longitude). The equipment at this site, the University of Utah Mobile Polarization Lidar and a surface radiation station from the Lamont-Doherty Geological Observatory of Columbia University, were taking part in the Intensive Field Observation phase of the FIRE [First ISCCP (International Satellite Cloud Climatology Program) Regional Experiment] Project (Starr, 1987).

2. Procedures

a. Lidar Observations

Dual-channel polarization lidar measurements were collected in the zenith direction from 1545-1700 (all times are GMT) in a low-PRF surveillance mode of 1 shot every 5 to 10 min, or generally every 2.5 min when cirrus clouds were detected. The ruby laser transmitter (0.694 μm wavelength) emits up to 1.5 J per pulse, and the lidar returns are digitized and stored at a resolution in range of 7.5 m (see Sassen, 1984). Although system parameters are routinely monitored, the system constant is not accurately known, and to derive quantitative data values from laser backscattering, each of the nineteen returns collected during this period has been treated using the analysis described below.

The analysis attempts to derive the isotropic volume backscatter coefficient β_c $(km\ sr)^{-1}$ attributable only to cirrus cloud particles, so that the volume extinction coefficient σ_c (km^{-1}), which is assumed to be linearly related to β_c, and the cloud optical thickness τ_c at the laser wavelength can be computed. For an uncalibrated lidar system, all operational parameters and constants can be grouped into the system constant term **C** and the lidar equation expressed as

$$S(z)\ z^2 = \mathbf{C}\ \beta_t(z)\ \exp\left[-2\int_0^z \sigma_t(z)\ dz\right] , \qquad (1)$$

where $S(z)\ z^2$ is the height-normalized relative returned signal. The subscript t refers to total quantities in a multiple component system, which can include contributions from molecular m, aerosol a, and cloud c constituents. The molecular scattering coefficients, derived from Rayleigh scattering formulas, are functions of wavelegnth and air density ρ $(g\ m^{-3})$, and at the ruby laser wavelength are obtained from $\beta_m(z) = 4.395 \times 10^{-7}\ \rho(z)$ and $\sigma_m(z) = (8\pi/3)\ \beta_m(z)$,

as in Fernald et al. (1972).

Under the assumption that the background aerosol component is negligible in the upper troposphere, only molecular and cloud contributions need to be considered in our case. Then, at some height z_0 just below the base of the cloud assumed to contain only molecular scatterers, the solution to Eq. (1) for the cloud backscattering coefficient is given by

$$\beta_c(z) = \frac{G(z_0,z)}{1 - 2\frac{\eta}{k}\int_{z_0}^{z} G(z_0,z')\,\partial z'} - \beta_m(z) \quad , \tag{2}$$

where

$$G(z_0,z) = \beta_m(z_0)\frac{S(z)\,z^2}{S(z_0)\,z_0^2}\exp\left[2\left(\frac{8\pi}{3} - \frac{\eta}{k}\right)\int_{z_0}^{z}\beta_m(\zeta)\,\partial\zeta\right] \quad ,$$

and the multiple scattering correction factor η and isotropic backscatter-to-extinction ratio k for cirrus cloud particles are taken, for computational purposes, as constants through the cloud layer (see Platt, 1979).

With knowledge of $\beta_c(z)$, the cloud optical thickness at the laser wavelength is obtained from

$$\tau_c = \frac{1}{k}\int_{z_b}^{z_t}\beta_c(z)\,dz \quad , \tag{3}$$

where z_b and z_t refer to cloud base and top heights. Moreover, the quantity $\beta_c(z)$ can be evaluated in terms of cloud microphysical content, i.e., the sum of the particle cross-sectional areas (times 4π when using the isotropic β) per unit volume, from

$$\beta_c(z) = g\,\pi^2\sum d_e^2\,N_i \quad , \tag{4}$$

where N_i is the concentration of particles, d_e the equivalent particle diameter,

and g the average backscattering gain factor appropriate for a distribution of ice crystal shapes and sizes (Sassen, 1978).

Concerning sources of error in the lidar-derived β_c and τ_c data, uncertainties are associated primarily with the selection of k and the assumption that $S(z)\ z^2$ at z_0 is due only to molecular scatterers of known density, particularly in the presence of weak signals. Table 1 provides values of k and g obtained from laboratory and field scattering measurements and theoretical simulations. Although the range of k values shown is relatively wide, it is often possible to specify a more limited range of values from auxiliary data. In addition, since the exponential term in the function G(z) of Eq. (2) generally has a minor impact on the derivation of $\beta_c(z)$ for optically thin clouds, the results are relatively insensitive to the choice of k or η (assumed to be 0.75 for a simple diffraction model). In contrast, the choice of k has a linear

Table 1. Values of the isotropic backscatter-to-extinction ratio k (per 4π steradian) and parallel-polarized backscattering gain g for ice clouds obtained by various investigators.

Reference	k	g	Comments
Sassen, 1978	0.04	0.007	Laboratory ice clouds
	0.26	0.04	Spatial ice crystals
	0.40	0.06	Crystal aggregates
Sassen and Liou, 1979	0.10	0.015	Laboratory ice clouds
Platt et al., 1987	0.16	----	Midlatitude cirrus, -60°C
	0.20	----	Tropical cirrus, -40 to -80°C
Takano, 1987*	0.026	0.004	Theoretical, thin plate crystals
	0.086	0.014	Theoretical, thick plate crystals
	0.038	0.006	Theoretical, long column crystals

*Personal communication.

impact on τ_c according to Eq. (3). The basic uncertainty in $\beta_c(z)$ values has been minimized by calculating $\beta_m(z)$ on the basis of an atmospheric density profile obtained from a rawinsonde launched from the site at 1200, and by appropriate signal averaging to reduce the impact of noise in determining $S(z)\ z^2$ at z_0. Shown in Fig. 1 is a typical profile of height-normalized returned signal, which is compared to a predicted curve based on pure molecular scattering.

Finally, again assuming that $\beta_t(z) = \beta_c(z) + \beta_m(z)$, lidar linear depolarization ratios δ_c for the cirrus cloud are derived from the parallel (||) and orthogonal ($\perp$) backscattering channels from the relation

$$\delta_c(z) = \frac{\beta_t(z)_\perp}{\beta_t(z)_{||} - \beta_m(z)_{||}} \quad , \tag{5}$$

where the essentially nondepolarized ($\delta_m \approx 0.02$) molecular scattering contributions are removed to obtain a value attributable only to the weakly-scattering cirrus clouds present on this occasion. The backscattering contributions from cloud particles are also expressed in relation to the molecular backscattering at the laser wavelength in terms of the scattering ratio,

$$R(z) = \frac{\beta_t(z)}{\beta_m(z)} \quad , \tag{6}$$

commonly used to characterize the presence of stratospheric aerosols.

b. Surface Flux Observations

Surface radiation measurements of the direct and diffuse components of the solar fluxes in the spectral interval from 0.28 to 2.8 μm were obtained from full hemispheric pyranometers. The diffuse component of the incident solar beam was obtained using a shadow band, after applying appropriate adjustments to the data. Radiation sensors were calibrated either prior to the FIRE experiment or on the basis of instrument intercomparisons with calibrated sensors during

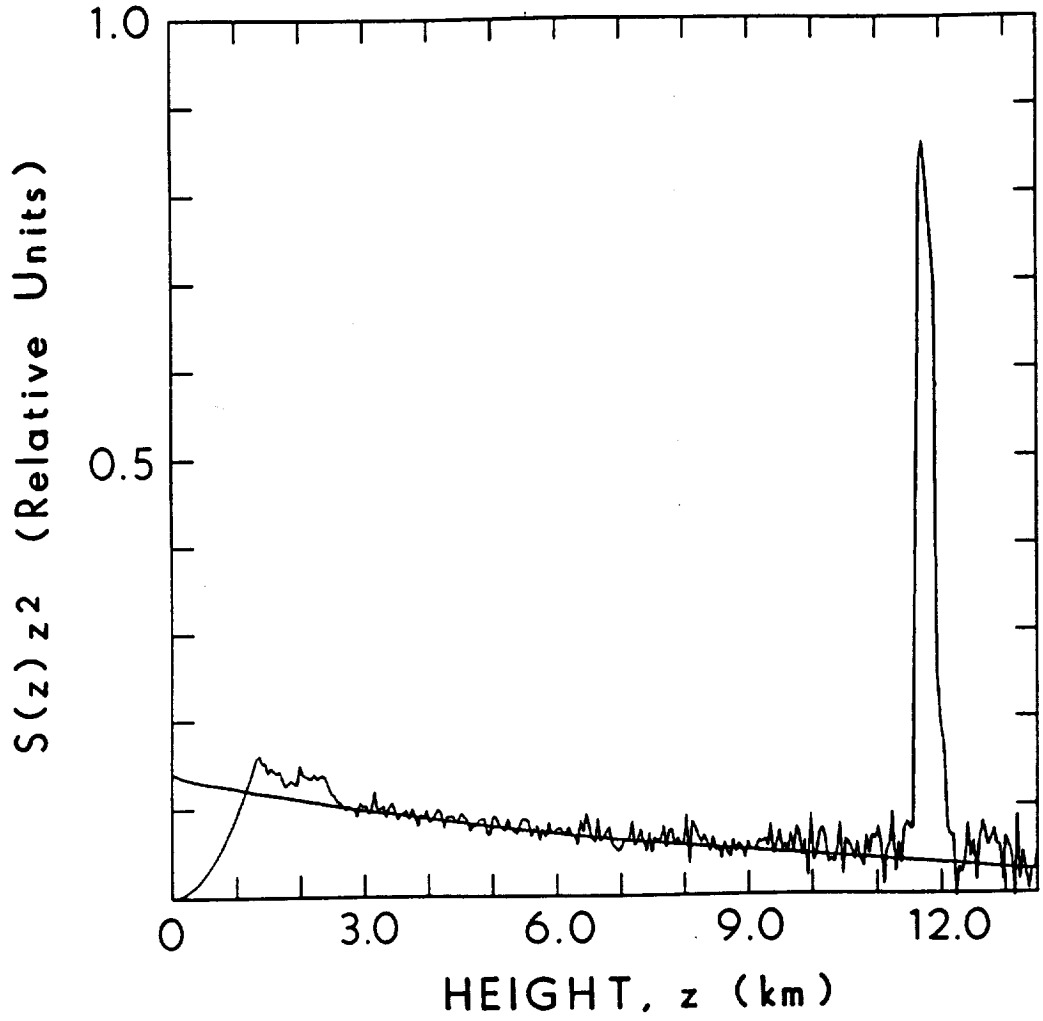

Fig. 1 Profile of height-normalized returned lidar signal for a single shot (at 1650 GMT) compared with predicted curve for pure molecular scattering, showing significant enhancements in backscattering from subvisual cirrus between 11.5-12.2 km (11.9-12.6 km MSL), and from aerosols within the boundary layer below 2.5 km. Lidar data are not valid below 1.3 km.

and following the field project.

The effective, shortwave optical thickness of the atmosphere in the direction normal to the earth's surface, τ, is computed using the following equation:

$$\tau = \mu_0 \ln \left[F_0/(F_S - F_{S,DIF})\right] \quad , \tag{7}$$

where μ_0 is the cosine of the solar zenith angle, F_0 is the solar irradiance at the top of the atmosphere, and F_S and $F_{S,DIF}$ are the total and diffuse shortwave fluxes received at the surface, respectively. F_0 is a function of latitude and time of day and year (i.e., solar declination), and is a maximum at local solar noon (the approximate time of observations).

Given in Fig. 2 are the records of calculated F_0 and measured F_S and $F_{S,DIF}$ over the three-hour period in GMT (local time = GMT - 5 h) bracketing the lidar observations. The flux measurements until about 1600 reflect dissipating fog conditions at the field site, and in comparison, the cirrus clouds that subsequently advected through the area can be seen to have had little effect on the flux values. Since our aim is to determine passively the nadir optical thickness τ_c due only to the extra attenuation produced by the cirrus, τ_c is estimated on the basis of the difference between the total atmospheric optical thickness derived from Eq. (7) and the τ to be expected without contributions from the cloud. This approach minimizes the impact of any systematic errors that might occur from sensor calibration uncertainties.

c. Photographs of Solar Corona

Although the initial cirrus did not generate any noticeable optical phenomena, the zenith-subvisual cirrus became visible as it drifted beneath the solar disk due to strong forward-scattering, and solar corona with two sets of colored rings were observed. Color slides of the corona were taken between

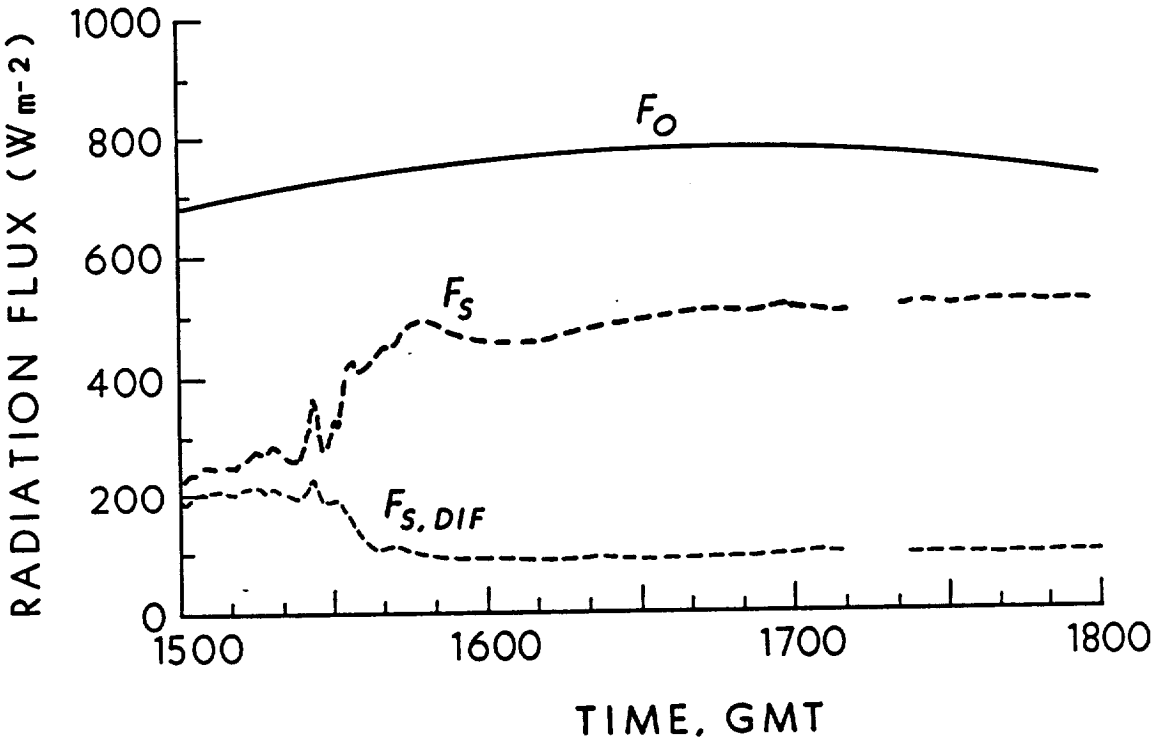

Fig. 2 Records of calculated solar irradiance at the top of the atmosphere F_0, and the total F_S and diffuse $F_{S,DIF}$ shortwave fluxes received at the surface. A 9 min data gap occurs at 1710.

1700-1715, and have been analyzed by measuring the angular positions of the red bands relative to the sun using enlargements of the images. Table 2 provides the angular separations θ_r between the centers of the red bands and the sun for four photographs analyzed in this fashion.

As described in Sassen (1979), the angular separations of coronal red bands from the sun can be related to the diameter d of the particles causing the optical display on the basis of simple diffraction-corona theory, as follows:

$$\sin\theta = (n + 0.22)\ \lambda/d \quad , \tag{8}$$

where θ refers to the angular separation of a corona minima of order n (corresponding to the dark bands of the diffraction pattern). It is customary to use a wavelength $\lambda = 0.57$ μm for the coronal red band maxima, which roughly correspond to the minima for green light. By definition, the occurrence of a colored solar corona provides evidence for a nearly monodispersed population of relatively small cloud particles, which are spherical or near-spherical in cross section. The equivalent diameters d_e of cirrus particles that fit the corona photograph analyses are included in Table 2.

Table 2. Angular separation θ_r between the sun and the first (n = 1) and second (n = 2) order corona red bands and effective particle diameter and average diameter $\bar{d}_e$, derived from four solar corona photographs.

	n = 1		n = 2		
	θ_r (°)	d_e (μm)	θ_r (°)	d_e (μm)	$\bar{d}_e$ (μm)
No. 1	1.62	24.6	3.00	24.2	24.4
No. 2	1.77	22.5	2.92	24.8	23.7
No. 3	1.60	24.9	2.66	27.3	26.1
No. 4	1.62	24.6	2.67	27.2	25.9

3. Results

Vertically-pointing lidar data are given in Fig. 3 in the form of height-versus-time displays of the scattering ratio R and linear depolarization ratio δ_c. To aid in the rejection of spurious data dominated by signal noise, 45-m (6 digitized data point) averages have been used, a threshold of R = 2.5 is employed to define the cloud boundaries, and δ values are computed for $R \geq 5.0$. Both the structure and depolarizing properties of the subvisual (1545-1610) and zenith-subvisual (1625-1700) cirrus clouds can be seen to differ rather significantly. The former cloud, which was not observed in its entirety, tends to display a layered structure and low δ values, while the latter displays a rather concentric arrangement of scattering ratio contours and δ values that are more typical of cirrus clouds. The overall appearance of the zenith-subvisual cloud is quite similar to that of long-lasting aircarft contrails that we have observed previously. Note also the presence of very weakly-scattering layers that straddle the tropopause height (the line at 12.78 km) and extend into the lower stratosphere. Although individual δ values derived from these weak signals are unreliable, layer-integrated ratios are typically ~0.35, indicating that the stratospheric layers were also composed of ice crystals. These layers normally contribute negligibly to the optical thickness of the cirrus clouds below, and are excluded from our analysis.

The total atmospheric optical thickness over the 1600-1800 period of interest, derived from the shortwave flux measurements is shown in Fig. 4 in terms of zenith-normalized values. On the basis of local rawinsonde sounding data, we have calculated a molecular optical thickness $\tau_m = 0.08$ over the corresponding spectral interval, indicating that the decreasing trend in τ_t is attributable to a lessening impact from haze particle scattering in response to gradual boundary layer heating. With the assumption that the minima of the τ

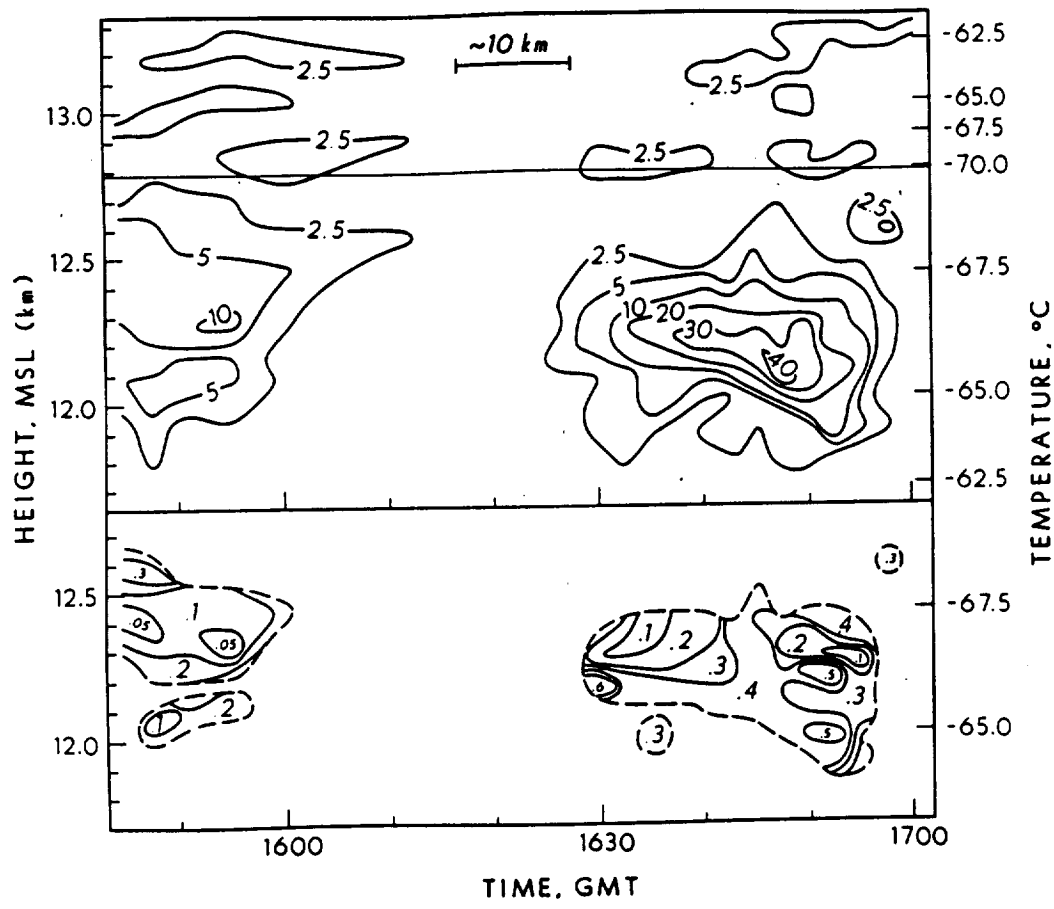

Fig. 3 Height-time display of lidar data showing the passage of the subvisual cirrus clouds. Scattering ratio R = 2.5 defines cloud boundaries (top), and linear depolarization ratios δ_c (bottom, where, e.g., a value of .3 represents $\delta_c = 0.3 \pm 0.05$) are computed only when $R \geq 5.0$. Temperatures are from the local 1200 GMT sounding.

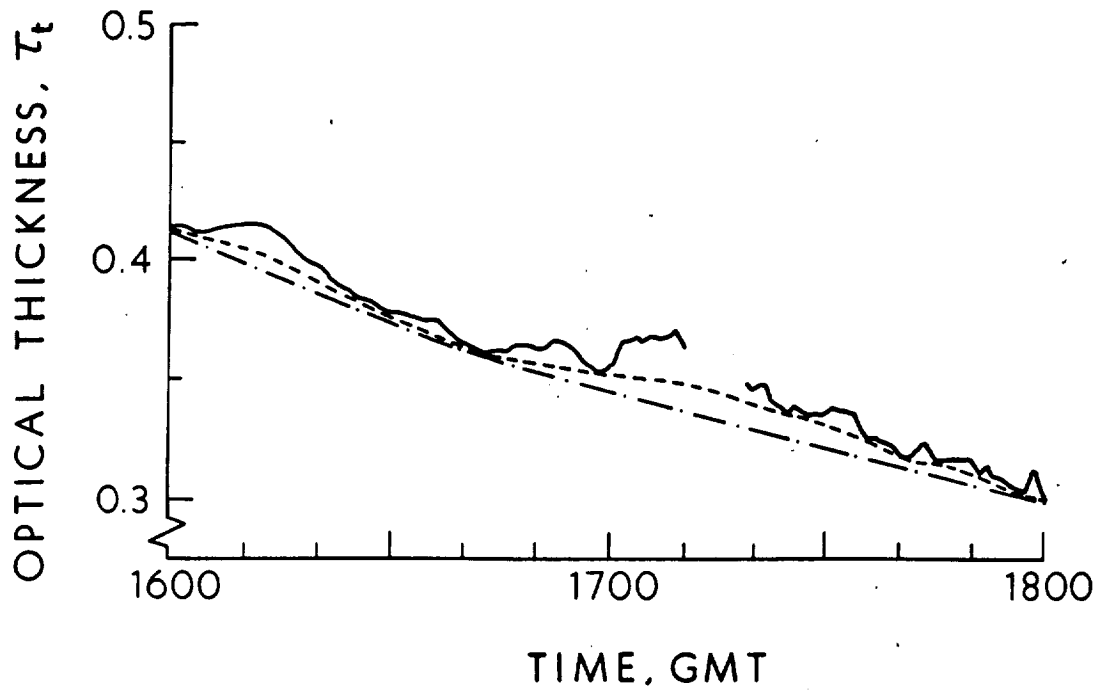

Fig. 4 Total nadir atmospheric optical thickness derived from shortwave flux data during the passage of the cirrus (solid line). Dashed lines for two "cloudless" scenarios are used to estimate the τ_c attributable to the cirrus alone.

variations represent the combined contributions of molecular and haze scatterers, as depicted by the dashed lines for two "cloudless" scenarios, it is then possible to estimate the increment in optical thickness due to the cirrus. The results of this analysis are compared to lidar-derived τ_c in Fig. 5.

In Fig. 5 the time scale of the radiometric τ_c record has been offset from the lidar data by 20 min to account for the advection time associated with cloud movement between the zenith and solar elevation angles. This estimate is based on the 16 m s^{-1} mean cirrus level wind speed, and is in general agreement with visual observations of the movement of visible portions of the cirrus. The two radiometrically-derived data records reflect the uncertainty in determining a "cloudless" optical thickness from τ_t in Fig. 4. The range of lidar-derived τ_c data values, shown by bars for each interrogation, corresponds to the uncertainty associated with the choice of k. We have chosen a 0.05-0.10 range of k values as being representative of the relatively small, simple ice crystals that the corona analysis indicates were present on this occasion, in compliance with the range of laboratory and theoretical values in Table 1. Although the cloud properties could naturally be expected to display both spatial and temporal variations, it is clear that both analysis methods yield comparable τ_c values. Given the sizes of the constituent cloud particles, which are relatively large in comparison to visible light wavelengths (see Table 2), differences between the broadband shortwave radiometric and monochromatic 0.694 μm-wavelength lidar data should not be significant.

Concerning the microphysical composition of the zenith-subvisual cirrus cloud band, inferences can be drawn from the combined passive photographic and active remote sensing observations. Although the solar corona analysis indicates that the responsible cloud particles were near-spherical in cross section and ~25 μm in effective diameter, the degree of linear depolarization

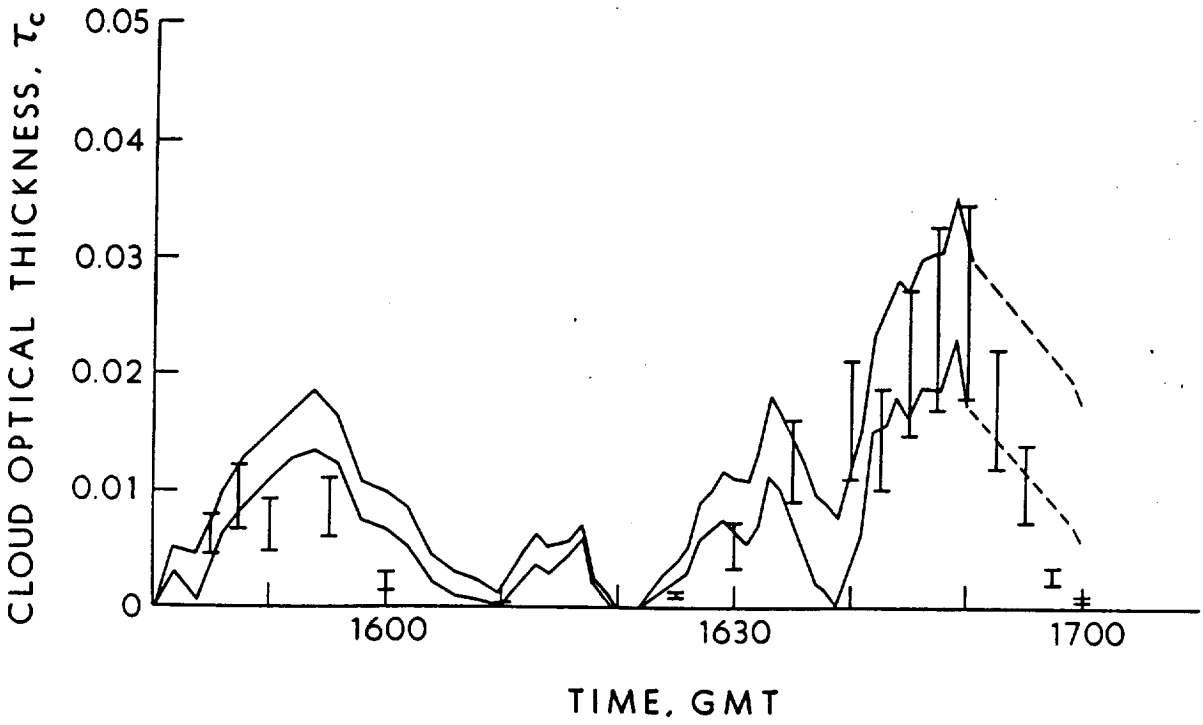

Fig. 5 Comparison of τ_c derived from lidar data (bars for each shot correspond to k = 0.05 and 0.1), and the two "cloudless" curves in Fig. 4 derived from shortwave flux data. Time applies to lidar observations, with the radiometric data offset by -20 min to allow for cloud movement.

measured by the lidar (Fig. 3), on the other hand, is consistent with hexagonal ice crystal scatterers typical of cirrus clouds. These contrasting observations, however, can be reconciled if it is assumed that the thick plate ice crystal habit was dominant. Such particles display hexagonal-symmetry scattering properties and yet may have an axial (thickness-to-diameter) ratio of close to unity to satisfy diffraction theory. The relatively small sizes of the particles are quite atypical of cirrus clouds (Heymsfield and Platt, 1986), but it should be recognized that little is currently known of the character of ice crystals at these extremely cold temperatures (-60 to -70°C) and low pressures (~200 mb). It should also be noted that the subvisual cirrus probed prior to 1610 display much lower δ values, indicating a difference in particle shape or composition.

With the knowledge of the mean particle sizes obtained passively, Eq. (4) can be employed to calculate the cirrus particle concentrations corresponding to the mean and maximum observed β_c in the zenith-subvisual cirrus. From Table 1, a backscattering gain $g = 0.01$ can be taken as representative of small, simple ice crystals, with an uncertainty of about a factor of two. Although the maximum $\beta_c = 6.4 \times 10^{-3}$ (km sr)$^{-1}$ value (averaged over 45 m) corresponds to a peak crystal concentration of ~110 ℓ^{-1}, the cloud layer average value of 1.4×10^{-3} (km sr)$^{-1}$ amounts to ~25 ℓ^{-1}. Similarly, maximum and mean values for the ice mass content M_i are 0.9 and 0.2 mg m^{-3}, and for the vertical cloud thickness Δz, 0.95 and 0.65 km, respectively.

4. Conclusions

The passive and active remote sensing dataset collected on this occasion has provided a unique opportunity to assess the optical thickness of an ice cloud that verged on becoming visible in the zenith viewing direction. The

atmospheric conditions prevailing during the experiment are nearly ideal for evaluating this threshold value, although the surface radiation data were affected by gradually diminishing extinction due to haze dissipation within the boundary layer. Since the observations were collected near local noon and portions of the main cirrus cloud band could be tracked visually against the otherwise cloud-free sky, the lidar and surface radiation measurements can be reliably related. Moreover, we have taken advantage of an unexpected auxiliary measurement of cirrus particle sizes made possible by solar corona effects. To the best of our knowledge, this is the first time that ice crystals have been unambiguously demonstrated to produce the colored corona optical phenomenon.

Compiled in Table 3 are the derived optical and microphysical quantities in terms of mean and maximum values corresponding to the subvisual and zenith-subvisual cirrus cloud observation periods. With regard to the second category, which is of primary interest, we can assign a $\tau_c \approx 0.03$ value as a threshold optical thickness for subvisual versus visual cirrus at the ruby laser wavelength. This threshold optical thickness compares favorably with the $\tau_c = 0.06$ reported by Platt et al. (1987) for a cirrus that was visible but very hazy in appearance. We further have estimated that, on average, these cloud particles were comprised of relatively small hexagonal ice crystals of ~25 μm effective diameter at typical concentrations of ~25 ℓ^{-1}.

It is important to recognize, however, that these findings correspond only to a type of subvisual cirrus cloud. Judging by the structure and aspect of the cirrus cloud band, it is probable that it was derived from an aircraft contrail, although the subvisual cirrus observed earlier displayed contrasting characteristics and may have formed naturally. Regardless of the formation mechanism, the clouds were observed to occur at very cold tropospheric temperatures (between -60 to -70°C) and to occupy a position just below the tropopause

Table 3. Mean and maximum optical and microphysical properties for subvisual cirrus and zenith-subvisual cirrus derived from ruby lidar (0.694 μm) probing from 1545-1600 (5-shot average) and 1630-1700 (10-shot average), and surface shortwave (0.28-2.8 μm) flux data from 1605-1620 and 1650-1710 GMT, respectively. Symbols defined in text.

	Surface Flux[1]	Lidar[2]					Photographic + Lidar		
	τ_c	τ_c	R	β_c $(km\ sr)^{-1}$	Δz km	δ_c	d_e μm	N_i ℓ^{-1}	M_i $mg\ m^{-3}$
Subvisual Cirrus									
Mean	0.011	0.007	5.2	0.6×10^{-3}	0.77	0.19	--	---	---
Maximum	0.016	0.009	11.3	1.5×10^{-3}	1.00	(0.15)	--	---	---
Zenith-Subvisual Cirrus									
Mean	0.014	0.015	11.1	1.4×10^{-3}	0.65	0.35	25	25	0.2
Maximum	0.030	0.026	45.1	6.4×10^{-3}	0.95	(0.34)	25	110	0.9

[1] Values from the average of the two curves in Fig. 4.

[2] Mean values are computed over the cloud depth Δz defined by $R \geq 2.5$ ($R \geq 5.0$ for δ_c) using $k = 0.075$ and $g = 0.01$. Maximum values represent 45 m-averages. Values in parentheses refer to the average integrated depolarization ratio (Platt et al., 1987).

height. The occurrence of cirrus layers at the tropopause appears to be fairly common on the basis of findings from routine lidar stratospheric aerosol observations (Hall, personal communication), and it is not uncommon to find them represented in published lidar aerosol scattering ratio profiles (see, e.g., McCormick and Swissler, 1983). Recently, Heymsfield (1986) has described aircraft microphysical data from a subvisual tropical cirrus cloud present at

-83°C. The sizes of the plate and column crystals collected on slides ranged from about 5 to 50 μm, and it was noted that the smaller crystals displayed axial ratios of approximately unity. Although the concentrations and ice mass contents of the ice particles could not be determined accurately, mean values of 50 ℓ^{-1} and 0.1 mg m^{-3}, respectively, were estimated for the 0.5 km deep cloud. Hence, the estimated microphysical properties of the aircraft-sampled subvisual cloud and our zenith-subvisual case are rather similar, although our data indicate a somewhat greater vertical cloud depth.

Our regular cirrus observations in support of the FIRE Project Extended Time Observations indicate that subvisual cirrus are also common whenever some cirrus cloud elements are observed visually. In other words, under broken or scattered ceiling conditions, the visible clouds represent enhanced concentrations of cirrus particles, which are commonly also distributed over extended regions that appear to be cloudless. These cirrus particles can form at a variety of atmospheric temperatures, and presumably can display a wide range of k and g values (see Table 1) that would affect the relationship between cloud visibility and lidar-derived τ_c. Moreover, plate crystals, when horizontally-oriented, produce an anisotropic scattering medium that greatly enhances the parallel-polarized laser backscattering collected in the zenith direction, often producing near-zero δ values (Sassen, 1984). These conditions also appear to be fairly common in cirrus, but it should be noted that the crystals must be a minimum of 200-300 μm diameter in order to display uniform orientations (Sassen, 1980). Oriented plate crystal scattering effects could have been responsible for the low δ values measured in the subvisual cirrus, but since the crystals would have had to be considerably larger than those producing the solar corona effects, it is also possible that this weakly scattering cloud was composed of a combination of spherical aerosols (i.e., haze droplets) and small ice crystals.

Although our findings describe only a single occurrence of subvisual cirrus clouds, general comparisons with the properties of stratospheric aerosol layers of volcanic origin and polar stratospheric clouds (PSC), which have been variously examined with regard to possible climatic impacts, can be made. These aerosol and cloud layers are generally 5-10 km in thickness with a centroid located within a 18-25 km range of altitudes in the lower stratosphere. On the basis of ground-based and airborne ruby lidar studies, maximum scattering ratios of 5-15 are found in PSC (Kent et al., 1986; Poole, 1987), while values as high as 10-45 have been observed following a major injection of volcanic aerosols such as accompanied the El Chichon eruption in April 1982 (McCormick and Swissler, 1983). In terms of cloud optical thickness, Stratospheric Aerosol Measurement (SAM) II observations at 1.0 μm obtained at high latitudes from the Nimbus 7 platform (McCormick and Trepte, 1987) show winter maxima of $\tau \approx 0.01$ due to PSC formation, while volcanic aerosol τ range from estimates of as high as 0.02-0.11 following El Chichon to ~0.005 in the post-Mt. St. Helens period. Based on lidar studies, a $\tau \approx 0.03$ (at 0.55 μm) was derived as a mean value for the post-Fuego stratospheric aerosol content (Russell and Hake, 1977). Polarization lidar observations of stratospheric aerosols reveal scattering properties that resemble those of both spheres and ice crystals, depending on temperature and cloud particle chemistry (Iwasaka and Hayashida, 1981; Poole, 1987).

In comparison, the $\tau < 0.03$ reported here for subvisual cirrus clouds correspond to the effects produced by relatively stong episodes of stratospheric aerosol loading, which occur rather infrequently. Subvisual cirrus, on the other hand, may be a far more regular feature of the upper troposphere, judging by recent Stratospheric Aerosol and Gas Experiment (SAGE) findings (Woodbury and McCormick, 1986). In that study the distribution of cirrus clouds was assessed,

including a category of optically thin cirrus displaying extinction coefficients at 1.0 μm between $8x10^{-4}$ to $8x10^{-3}$ km^{-1}. Such σ values are comparable to those that can be derived from the β_c values for our subvisual cirrus case, and the SAGE data indicate that these conditions occur, on a nearly global average, at a frequency of about 15%. Although increased knowledge of the properties and frequency of occurrence of subvisual cirrus is clearly required for a proper assessment of their climatic impact, these findings suggest that the effects produced by these tenuous clouds could represent a relatively significant component in the radiation balance of the earth-atmosphere system. Further experimental studies and theoretical radiative transfer simulations are warrented in order to obtain a more complete understanding of this problem, including the possible climatic perturbations induced by the relatively recent appearance of subvisual cirrus from aircraft contrails.

References

Fernald, F.G., B.M. Herman and J.A. Reagan, 1972: Determination of aerosol height distributions by lidar. J. Appl. Meteor., 11, 482-489.

Heymsfield, A.J., 1986: Ice particles observed in a cirriform cloud at -83°C and implications for polar stratospheric clouds. J. Atmos. Sci., 43, 851-855.

Heymsfield, A.J. and C.M.R. Platt, 1984: A parameterization of the particle size spectrum of ice clouds in terms of the ambient temperature and the ice water content. J. Atmos. Sci., 41, 846-855.

Iwasaka, Y. and S. Hayashida, 1981: The effects of the volcanic eruption of St. Helens on the polarization properties of stratospheric aerosols: Lidar measurements at Nagoya. J. Meteor. Soc. Japan, 59, 611-614.

Kent, G.S., L.R. Poole and M.P. McCormick, 1986: Characteristics of arctic polar stratospheric clouds as measured by airborne lidar. J. Atmos. Sci., 43, 2149-2161.

McCormick, M.P. and T.J. Swissler, 1983: Stratospheric aerosol mass and latitudinal distribution of the El Chichon eruption cloud for October 1982. Geophys. Res. Lett., 10, 877-880.

McCormick, M.P. and C.R. Trepte, 1987: Polar stratospheric optical depth observed between 1978 and 1985. J. Geophys. Res., 92, 4297-4306.

Platt, C.M.R., 1979: Remote sounding of high clouds: I. Calculation of visible and infrared optical properties from lidar and radiometer measurements. J. Appl. Meteor., 18, 1130-1143.

Platt, C.M.R., J.C. Scott and A.C. Dilley, 1987: Remote sounding of high clouds. Part VI: Optical properties of midlatitude and tropical cirrus. J. Atmos. Sci., 44, 729-747.

Pollack, J.B. and C.P. McKay, 1985: The impact of polar stratospheric clouds on the heating rates of the winter polar stratosphere. J. Atmos. Sci., 42, 245-262.

Poole, L.R., 1987: Airborne lidar studies of arctic polar stratospheric clouds. Ph.D. Dissertation, University of Arizona, 217 pp.

Russell, P.B. and R.D. Hake, 1977: The post-Fuego stratospheric aerosol: Lidar measurements, with radiative and thermal implications. J. Atmos. Sci., 34, 163-177.

Sassen, K., 1978: Backscattering cross sections for hydrometeors: Measurements at 6328 A. Appl. Opt., 17, 804-806.

Sassen, K., 1979: Iridescence in an aircraft contrail. J. Opt. Soc. Am., 68, 1080-1083.

Sassen, K., 1980: Remote sensing of planar ice crystal fall attitudes. J. Meteor. Soc. Japan, 58, 422-429.

Sassen, K., 1984: Deep orographic cloud structure and composition derived from comprehensive remote sensing measurements. J. Clim. Appl. Meteor., 23, 568-583.

Sassen, K. and K.N. Liou, 1979: Scattering of polarized laser light by water droplet, mixed phase and ice crystal clouds: II. Angular depolarizing and multiple scattering behavior. J. Atmos. Sci., 36, 852-861.

Starr, D.O'C., 1987: A cirrus-cloud experiment: Intensive field observations planned for FIRE. Bull. Amer. Meteor. Soc., 68, 119-124.

Woodbury, G.E. and M.P. McCormick, 1986: Zonal and geographical distributions of cirrus clouds determined from SAGE data. J. Geophys. Res., 91, 2775-2785.